small methods
www.small-methods.com

Synthesis of High-Performance Monolayer Molybdenum Disulfide at Low Temperature

*Ji-Hoon Park, Ang-Yu Lu, Pin-Chun Shen, Bong Gyu Shin, Haozhe Wang, Nannan Mao, Renjing Xu, Soon Jung Jung, Donhee Ham, Klaus Kern, Yimo Han, and Jing Kong**

The large-area synthesis of high-quality MoS_2 plays an important role in realizing industrial applications of optoelectronics, nanoelectronics, and flexible devices. However, current techniques for chemical vapor deposition (CVD)-grown MoS_2 require a high synthetic temperature and a transfer process, which limits its utilization in device fabrications. Here, the direct synthesis of high-quality monolayer MoS_2 with the domain size up to 120 µm by metal-organic CVD (MOCVD) at a temperature of 320 °C is reported. Owing to the low-substrate temperature, the MOCVD-grown MoS_2 exhibits low impurity doping and nearly unstrained properties on the growth substrate, demonstrating enhanced electronic performance with high electron mobility of 68.3 $cm^2 V^{-1} s^{-1}$ at room temperature. In addition, by tuning the precursor ratio, a better understanding of the MoS_2 growth process via a geometric model of the MoS_2 flake shape, is developed, which can provide further guidance for the synthesis of 2D materials.

1. Introduction

Monolayer molybdenum disulfide (MoS_2), a member of 2D transition metal dichalcogenides (TMDs), has attracted significant interest in scientific and engineering fields for pursuing emerging technologies including wearable electronics, ultimately scaled transistors, artificial synaptic devices, and optoelectronics due to its atomically thin thickness, sizable bandgap, large excitonic effect, and dangling-bond-free interface.[1–5] This explosive attention for MoS_2 has created a new demand for the synthesis of monolayer MoS_2 with large area, high uniformity, and high quality. Since 2012, high-crystallinity monolayer MoS_2 has been synthesized via thermal chemical vapor deposition (CVD) method using sulfur (S) and molybdenum trioxide (MoO_3) powders as the precursors (referred to oxide-based CVD throughout this work).[6–8] Despite the rapid progress in the growth of 2D TMDs over the past decade, methods for deposition of high-quality monolayer MoS_2 directly on the target substrates with a low thermal budget are still lacking, which would hamper its full potential in various applications. For example, the future ultrahigh-integration-density monolithic 3D CMOS architecture requires a process temperature lower than 400 °C to construct the desired structures and prevent issues such as dielectric degradation, electrical contact deterioration, and dopant diffusion in the lower tiers.[9–12] To date, attempts at growing MoS_2 at low temperatures (<400 °C) have been still limited by a low carrier mobility (<10 $cm^2 V^{-1} s^{-1}$), as summarized in Table S1 (Supporting Information).[13–16] Since a typical CVD process for preparing monolayer MoS_2 requires a high synthetic temperature of >700 °C, the state-of-the-art solution is to introduce an additional transfer process in which the as-grown monolayer MoS_2 is mechanically and/or chemically detached from the original growth substrate and placed on the target substrate.[17–20] However, the transfer process often induces mechanical damages on MoS_2 such as wrinkles, voids, and cracks or impurity residues (e.g., poly(methyl methacrylate) (PMMA), potassium hydroxide (KOH)) that degrade the quality of the material.[21]

Furthermore, the amount of vaporized precursors of Mo and S is difficult to evaluate and control, which brings challenges to the optimization of the growth result and sometimes even the reproducibility of synthesis in the oxide-based CVD process. Hence, it is highly desirable to develop low-temperature, and high-quality MoS_2 synthesis processes addressing these challenges. In this regard, Kang et al. demonstrated preparation for continuous monolayer MoS_2 via the metal-organic CVD (MOCVD) method at a relatively low temperature (≈550 °C).[22]

Dr. J.-H. Park, A.-Y. Lu, Dr. P.-C. Shen, Dr. H. Wang, Dr. N. Mao, Prof. J. Kong
Department of Electrical Engineering and Computer Science
Massachusetts Institute of Technology
Cambridge, MA 02139, USA
E-mail: jingkong@mit.edu

Dr. J.-H. Park, Prof. J. Kong
Research Laboratory of Electronics
Massachusetts Institute of Technology
Cambridge, MA 02139, USA

Dr. B. G. Shin, Dr. S. J. Jung, Prof. K. Kern
Max Planck Institute for Solid State Research
Heisenbergstrasse 1, 70569 Stuttgart, Germany

R. Xu, Prof. D. Ham
School of Engineering and Applied Sciences
Harvard University
Cambridge, MA 02138, USA

Prof. K. Kern
Institut de Physique
École Polytechnique Fédérale de Lausanne (EPFL)
1015 Lausanne, Switzerland

Prof. Y. Han
Department of Materials Science and NanoEngineering
Rice University
Houston, TX 77005, USA

The ORCID identification number(s) for the author(s) of this article can be found under https://doi.org/10.1002/smtd.202000720.

DOI: 10.1002/smtd.202000720

Nevertheless, the grain size was still limited to a few micrometers. Several following studies confirmed the challenges of decreasing nucleation density and increasing grain size of MoS_2 flakes in the MOCVD process.[23–25] Based on our observations, it is difficult to control the evaporation of molybdenum hexacarbonyl ($Mo(CO)_6$) as the solid metal-organic precursor of Mo, due to its complicated decomposition process and multiplex intermediate products.[26,27] On the basis of their work, we demonstrate that a steady flow rate of $Mo(CO)_6$ in the nucleation stages is an important factor toward high-quality MoS_2 deposition with a large domain size, and provide a deeper understanding of the growth mechanism.

In this work, we successfully synthesize monolayer MoS_2 on versatile substrates such as SiO_2/Si, sapphire, soda-lime glass, and gold film/SiO_2 by the MOCVD at a low temperature of 320 °C by designing the experimental setup for better controlling the flow rate of the organic precursors and thus the nucleation density. Large single-crystal monolayer MoS_2 with a domain size up to 120 µm can be obtained on SiO_2/Si substrate. In order to provide a comprehensive understanding of the growth mechanism of MOCVD-grown MoS_2, we apply a trigonometric function to quantitatively describe the shape change of MoS_2 flakes from a geometric perspective. Based on Raman spectroscopic characterizations, the MOCVD MoS_2 grown at a low temperature shows a lower electron doping and reduced tensile strain (≈0.15%) than those in our oxide-based CVD-grown counterpart, confirming the high quality of deposition. This enables a transfer-free fabrication process for 2D field-effect transistors (FETs) through the low-temperature deposition of monolayer MoS_2 channels directly onto the gate dielectric. The MoS_2 FETs exhibit an excellent electrical performance with an enhanced electron mobility as high as 68.3 $cm^2\ V^{-1}\ s^{-1}$ at room temperature. To the best of our knowledge, it is the highest mobility reported so far for monolayer MOCVD-grown MoS_2 as shown in Table S1 (Supporting Information).

2. Results and Discussion

MOCVD is an attractive route for large-area MoS_2 synthesis using $Mo(CO)_6$ and diethyl sulfide ($(C_2H_5)_2S$) as the Mo and S precursors, respectively. The precise control of the organic precursors is an important factor in the MOCVD for growing high-crystalline MoS_2 with a high reproducibility. Here, we develop a homemade MOCVD system with modified containers for the precursors, as shown in **Figure 1**a and Figure S1 (Supporting Information). The liquid sulfur precursor, $(C_2H_5)_2S$, is stably supplied by a typical bubbler system using argon as the carrier gas at room temperature (Figure S1a, Supporting Information). Compared to $(C_2H_5)_2S$, controlling the concentration and decomposition rate of solid $Mo(CO)_6$ is more challenging and important for decreasing nucleation density and increasing the domain size of MoS_2. Hence, we designed a solid bubbler system with a mesh grid filter and keep it at room temperature without any heating elements (Figure S1b,c, Supporting Information).[28] To further reduce the concentration of $Mo(CO)_6$, we flow argon as the carrier gas through the bubbler system. The substrates are placed in an upstream quartz tube near the furnace edge to maintain a low substrate temperature, which allows a low local decomposition rate of $Mo(CO)_6$ (more details in Supporting Information). As the temperature at the center of the quartz tube is set to 775 °C, the temperature at the substrate position is about 320 °C due to the temperature gradient of the furnace (Figure S2, Supporting Information). The low local temperature ensures the low decomposition rate of $Mo(CO)_6$ which allows decreasing nucleation density. It is noted that MoS_2 was not grown in the center of the quartz tube at a furnace temperature of 320 °C under the same flow conditions. This is attributed to the longer decomposition path of $Mo(CO)_6$ inside the quartz tube in such a scenario. It has been reported that $Mo(CO)_6$ decomposes around temperatures of 250 °C by the residual gas analyzer (RGA) study.[22,29] Figure S3a in the Supporting Information shows the MoS_2 thin film deposited on the inner wall of the quartz tube at the edge of the heating zone, which suggests that $Mo(CO)_6$ is consumed before arriving at the center of the quartz tube.

Figure 1b shows the optical images for monolayer MoS_2 grown at a substrate temperature of 320 °C on various substrates such as typical SiO_2/Si, gold thin film, and transparent insulating substrates such as sapphire, soda-lime glass, and thin borosilicate glass with 100 µm thickness (Figure S3b, Supporting Information). Through controlling the flow rate and thermal decomposition of precursors, large single-domain MoS_2 with the lateral size of 120 µm is achieved on SiO_2/Si. For metal substrates, gold is one of the few options for MoS_2 growth because of the formation of metal sulfide.[30] Our low-temperature deposition process enables monolayer MoS_2 to be grown on gold thin films (Au (50 nm)/Ti (5 nm) deposited on SiO_2/Si). Compared to metal and SiO_2/Si substrates, most transparent substrates exhibit the maximum stable temperature lower than 500 °C,[31] which is not suitable for conventional oxide-based MoS_2 CVD growth.[32,33] Hence, our low-temperature deposition process can potentially benefit the direct synthesis of TMDs on transparent substrates.

Figure 1c displays the Raman spectra of as-grown monolayer MoS_2 with two characteristic features of E_{2g} (≈383 cm^{-1}) and A_{1g} (≈403 cm^{-1}) vibrational modes without observable J1 mode (≈158 cm^{-1}) for 1T phase (Figure S4, Supporting Information)[34] on various substrates,[35,36] showing the frequency difference of ≈20 cm^{-1} for the evidence of a monolayer MoS_2 with 2H phase. The Raman shifts and the widths for MoS_2 on different substrates are listed in Table S2 (Supporting Information), verifying the successful growth of MoS_2 on these substrates. Also, the Raman spectra of the MoS_2 flakes do not contain the Raman peak of amorphous carbon which could be present as organic precursors are being used, indicating the purity of the as-grown MoS_2 crystals. Note that the amorphous carbon Raman peak can be observed under unoptimized growth conditions, as shown in Figure S5 (Supporting Information).[24] Figure S6 (Supporting Information) shows X-ray photoelectron spectroscopy (XPS) of as-grown monolayer MoS_2 on SiO_2/Si with the stoichiometric ratio of Mo:S = 1:2.12 and the binding energy of Mo^{4+} $3d_{5/2}$ at 229 eV for 2H characteristic feature. Figure S7a (Supporting Information) shows an atomic force microscopy (AFM) image with the thickness of 0.68 nm. Furthermore, Figure 1d,e show a scanning tunneling microscopy (STM)[37] image with honeycomb lattices without atomic defects and an annular dark-field scanning transmission electron microscopy

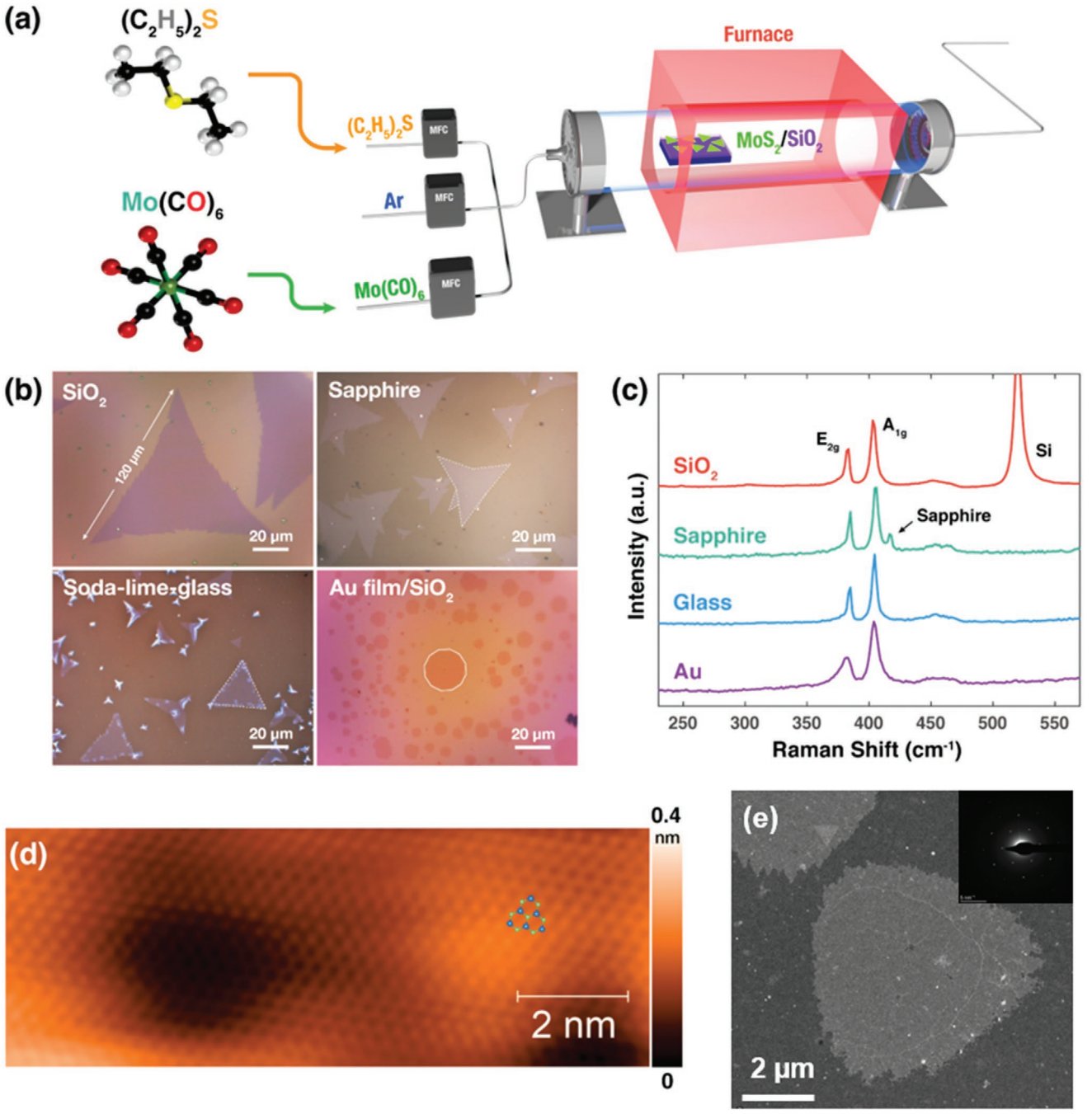

Figure 1. MOCVD-grown MoS_2 on various substrates at low temperature. a) Schematic diagram of the experimental setup of the homemade MOCVD system for MoS_2 growth. b,c) Optical images and Raman spectra of MoS_2 flakes grown on various substrates at low temperature of 320 °C. d) Atomic-resolution STM image of as-grown MoS_2 on SiO_2/Si substrate measured at the temperature of 4.9 K ($V_s = -3.5$ V; $I_t = 500$ pA). Bright protrusions as a honeycomb structure correspond to S atoms as inserted H-MoS_2 structure (green: S; blue: Mo). e) ADF-STEM image of single-crystal hexagonal MoS_2. The inset shows the diffraction pattern of MoS_2 with single crystallinity.

(ADF-STEM) image of single-crystal hexagonal MoS_2 with its diffraction pattern under dark-field TEM (DF-TEM), respectively, indicating the high crystallinity of monolayer MoS_2 grown at the low temperature. In addition, we demonstrate large area and high uniformity of continuous monolayer MoS_2 film on SiO_2 substrate with the size of 12×10 mm^2 prepared by placing the substrates vertically (Figure S9a, Supporting Information). Figure S9b–e (Supporting Information) displays Raman spatial maps for the intensities of A_{1g} and E_{2g} mode and PL spatial maps for the exciton positions and intensities, indicating the homogeneity of distribution.

In order to investigate the growth mechanism of MOCVD-grown MoS_2, especially understanding the effect of the location and temperature inside the furnace, we place multiple SiO_2/Si

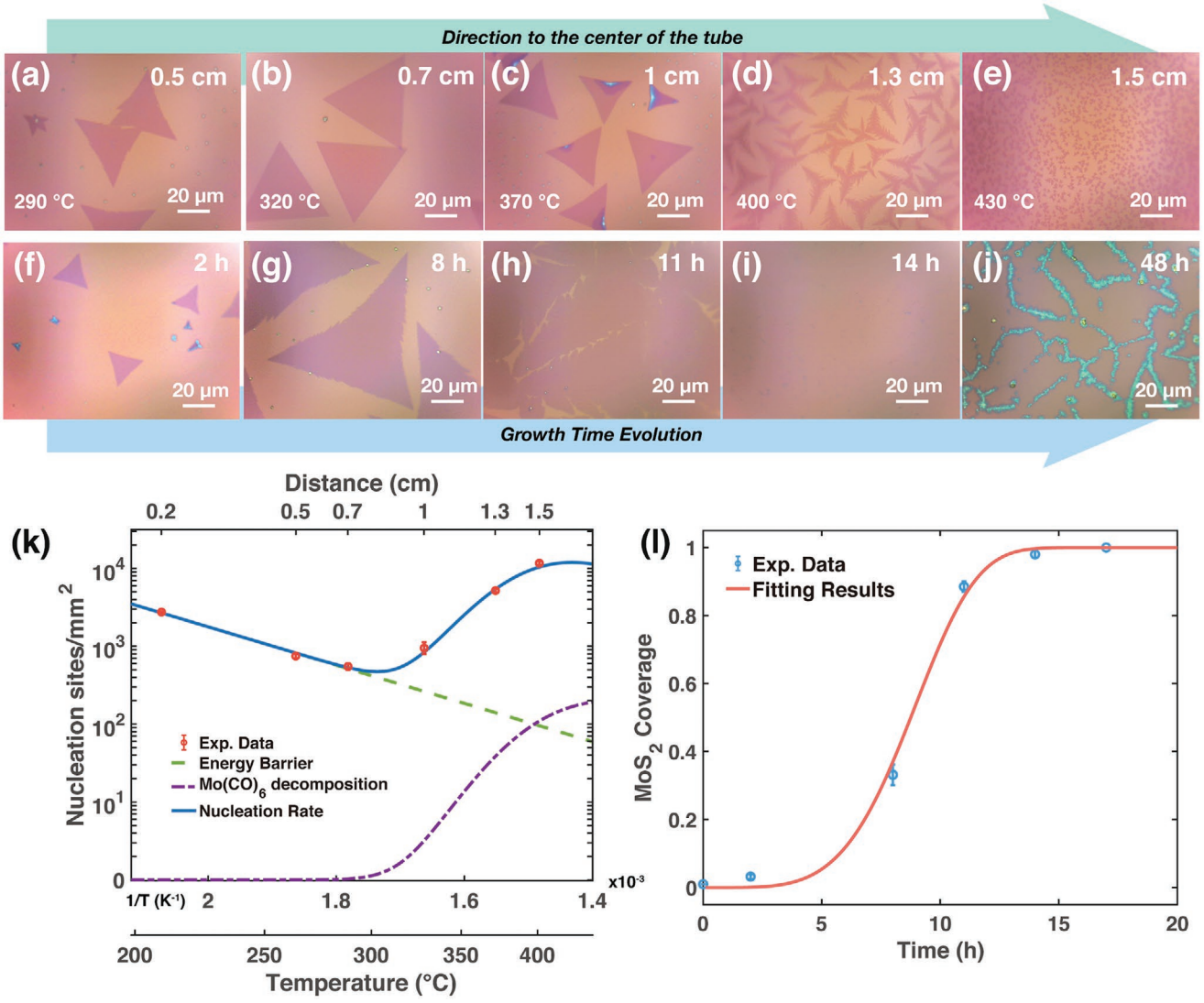

Figure 2. Effect of the growth temperature and growth time for MOCVD-grown MoS_2. a–e) Optical images of monolayer MoS_2 flakes obtained at different locations (with different local temperatures between 290 and 430 °C), with a growth time of 6 h. The starting point (0 cm) is at the edge of the furnace in the upstream location shown in Figure S2 (Supporting Information). f–j) Optical images showing the change from flake to a film of monolayer MoS_2 for different growth times at a low-temperature region of about 320 °C. k) The plot of the nucleation density as a function of temperature. l) The plot of MoS_2 coverage as a function of time.

substrates along the upstream locations inside the quartz tube. We utilize this method to monitor MoS_2 growth behavior such as domain size, geometries, coverage, and nucleation density. With the temperature gradient inside the furnace, these substrates experience different local temperatures. By measuring the temperature at five different locations, we adopt a finite difference (FD) method with trapezoidal time-marching to simulate the temperature profile in the quartz tube (Figure S2, Supporting Information) thus mapping out the temperature for all the locations inside the furnace. The temperature gradient increases dramatically at the edge of the furnace. **Figure 2**a–e shows monolayer MoS_2 on SiO_2/Si substrates at different locations, with growth temperatures ranging from 290 to 430 °C. As the location moves toward the center of the furnace and the temperature increases (which also corresponds to a longer $Mo(CO)_6$ decomposition path), the shapes of MoS_2 evolve from equilateral triangle in Figure 2a,b to concave polygon in Figure 2c–e. It is noted that the dendrite structure in Figure 2d is due to the diffusion-limited growth in the kinetic regime.[38] On the other hand, the nucleation density decreases first at a lower temperature region (220–290 °C) and then increases at a relatively higher temperature region (300–430 °C). This phenomenon is contradictory to previous studies[39] that the nucleation density decreases with increasing temperature. According to the classical nucleation theory, nucleation densities can be described as Equation (1)[40]

$$N = 2\pi r^* a_0 \sin\theta \frac{PN_A}{\sqrt{2\pi MRT}} n_s \exp\frac{E_{des} - E_s - \Delta G^*}{kT} \quad (1)$$

$$= A \cdot P(T) \cdot \exp\frac{E_{des} - E_s - \Delta G^*}{kT} \quad (2)$$

where N is the nucleation rate which is related with the nucleation density. r^*, a_0, and θ are the critical size, the height, and the contact angle of the nucleus of MoS_2, respectively. P is the partial pressure of Mo atomic species, N_A is Avogadro's number, M is the MoS_2 molecular weight, R is the gas constant, E_{des} is the energy required to desorb the molecules back into the vapor, and E_s is the activation energy for surface diffusion. For graphene growth via CVD, most models only consider the Arrhenius activation energy (the exponential term in Equation (2)) for nucleation density and set other factors as constants. This is because the decomposition probability of methane is nearly 1 (99.8%)[41] at high temperature (≈1000 °C), which thus can be regarded as a constant. However, in our MOCVD experiments, we observed that the inside of the quartz tubes was coated by a dark yellow layer of MoS_2 thin film in the temperature range of 200–500 °C (Figure S3a, Supporting Information), indicating the decomposition of $Mo(CO)_6$. Therefore, the nucleation density of MOCVD-grown MoS_2 is not only correlated to temperature (T) but also proportional to the partial pressure (P) of the precursors (Equation (2)). Here, we only take into account the partial pressure of Mo atomic species (Equation (3)), since the thermal decomposition of diethyl sulfide is almost invariable from room temperature to 550 °C[22]

$$P_{Mo} = P_{Mo(CO)_6} \times D_p \tag{3}$$

where P_{Mo} is the pressure of Mo atomic species, $P_{Mo(CO)_6}$ is the pressure of $Mo(CO)_6$, and D_p is the decomposition probability of $Mo(CO)_6$. Figure 2k shows the plot of the nucleation density as a nonmonotonic function of substrate temperature. Since average domain size equals surface coverage divides nucleation density, hence, the average domain size shows a reverse trend compared to the nucleation density (Figure S10, Supporting Information), which is consistent with the previous report.[21] The nucleation densities of MoS_2 at different temperatures are calculated from the optical microscopic images in Figure 2a–e and labeled as red dots in Figure 2k. The temperatures are estimated from the simulation in Figure S2 (Supporting Information) and validated by thermocouple measurements. As can be seen in Figure 2k, the Arrhenius activation energy can be fitted in the low-temperature region (the green line); the fitting result shows that the Arrhenius activation energy is 0.49 eV. After subtracting the Arrhenius activation energy part from the nucleation rate (the blue line) in Figure 2k, the pressure of Mo atomic species (P_{Mo}) can be obtained (the purple line). The decomposition probability (D_p) is plotted in terms of Gaussian cumulative distribution function as shown in Figure S11 (Supporting Information), which is consistent with the literature data of MoS_2 decomposition on quartz and silver substrates.[29]

Figure 2f–j presents optical images showing the MoS_2 coverage changes from individual flakes to a continuous film of monolayer MoS_2 at 320 °C. The lateral size of MoS_2 flakes grows from 20 µm (Figure 2f) at 2 h to over than 100 µm at 8 h (Figure 2g) and then the MoS_2 domains merge into a continuous monolayer film (Figure 2i) at 14 h. After 48 h, multilayer MoS_2 can be observed at locations likely the domain boundaries (Figure 2j), which implies that the boundaries and defects could be the nucleation sites for multilayer MoS_2 growth. In Figure 2l, we plot the coverage of MoS_2 as a function of time and fit by Avrami (JMAK) equation (Equation (4))[33]

$$A(t) = 1 - \exp\left[-K(T)t^n\right] \tag{4}$$

where $A(t)$ is the coverage of MoS_2, n is the Avrami exponent, which can be expressed as n = dimension + transformation type, and K is the rate constant. The transformation types include continuous nucleation and site saturation. Continuous nucleation represents nuclei added during growth and site saturation indicates all nuclei present at the very beginning (Figure S12, Supporting Information). From the fitting result, n equals 3.1, indicating the continuous nucleation for 2D crystal growth (more details concerning the JMAK equation are described in the Supporting Information). K is about 0.001 in our case, which corresponds to a slow reaction.

The MoS_2 flakes show different shapes under different growth conditions. Their shapes help us to understand the growth mechanism, since they are highly correlated to the Mo:S concentration ratio and the temperature in the synthesis environments.[8,42,43] Although the growth mechanism with qualitative analysis was proposed in previous studies,[8,42] the precursor concentration of Mo and S is difficult to evaluate from powder-based precursors which strongly depends on their locations and the evaporated temperatures. The MOCVD process makes it easier to control the flow rate of the precursors. Here, we propose a quantitative model for MoS_2 shape change from a geometrical perspective, and the schematic illustration is shown in **Figure 3**a–h. First, we calculate the ratio of the MoS_2 perimeter (solid line) to its equilateral triangle (dash line) (this is referred to as perimeter ratio (PR), the ratio is either negative (Mo-edge) or positive (S-edge) depending on the flake edge termination). Second, we correlate the PR to an angle measured from the vertex of a regular hexagon (black dots) relatively to the vertex of the equilateral triangle MoS_2 (thus with a range of −90° to 90°. The vertices are blue dots for Mo-edge and red dots for S-edge). Finally, the angle of MoS_2 flakes with the sulfur flow rate is projected to an arctangent curve, allowing us to investigate the growth behavior of monolayer MoS_2. From the schematic illustration in Figure 3a–h, a regular hexagon having sixfold symmetry (Figure 3a) evolves into a hexagon having threefold symmetry (Figure 3b), then into an equilateral triangle (Figure 3c), then a concave polygon (Figure 3d) as the sulfur concentration becomes increasingly dominant during the growth. The PR (solid line:dash line) of MoS_2 flakes rise from 0.67 (2:3) to 0.83 (2.5:3), 1 (3:3), and 1.04 (3.12:3), and the angles also increase from 0° to 30°, 60°, and 79°, respectively. Similar to the increase of sulfur concentration influence, the Mo-terminated MoS_2 transits from a regular hexagon to a concave polygon (Figure 3e–h) and the angle goes from 0° to −79° as the molybdenum concentration becomes increasingly dominant. From our experimental results in Figure 3i–n, the optical microscopic images display different shapes of MOCVD-grown MoS_2 fakes with various sulfur flow rates and a fixed molybdenum flow rate of 0.1 sccm at the same growth temperature and location of 0.7 cm. In Figure 3i, MoS_2 is grown in a sulfur-rich environment with a sulfur flow rate of 2.5 sccm, showing a concave polygon shape with the PR of 1.028. With the decrease of sulfur flow rates to 1.75 sccm (Figure 3k) and 1.25 sccm (Figure 3m),

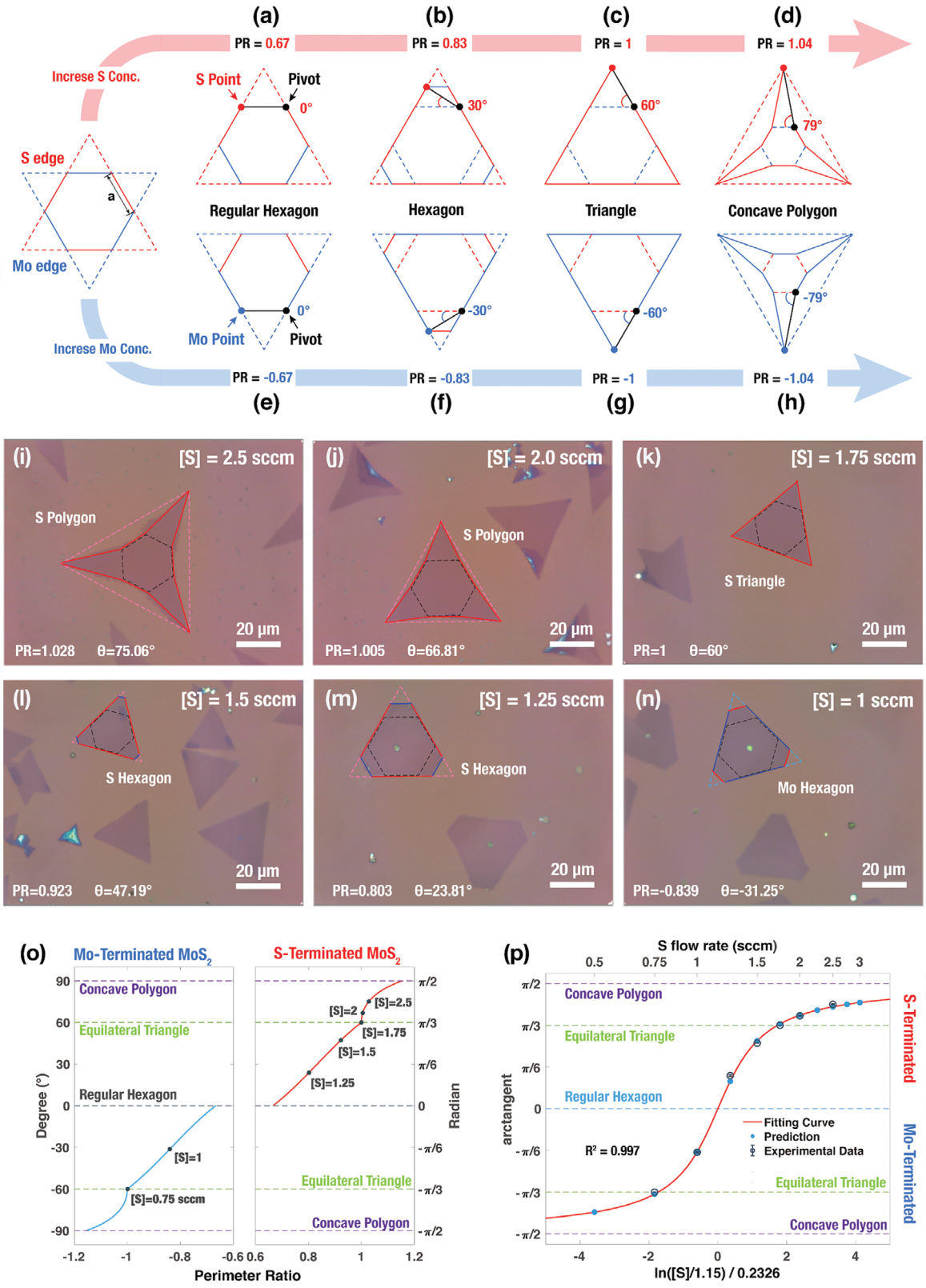

Figure 3. The shape change of MOCVD-grown MoS_2. a–h) The schematic illustration of the quantitative model for MoS_2 shape change from a geometrical perspective. For a hexagonal shaped MoS_2 flake, the red edge is S-terminated edge and the blue edge is Mo-terminated edge. i–n) Optical images display different shapes of MoS_2 with various sulfur flow rates. o) The plot of the angle dependence on the perimeter ratio (PR). p) The plot of the arctangent for the transition angle as a function of the sulfur flow rate.

the MoS_2 shape transits into an equilateral triangle with the PR of 1 and a hexagon with the PR of 0.803, respectively. According to the geometric calculation for hexagon and concave polygon in Figure S13 (Supporting Information), we plot the curve correlating the PR to the angle in Figure 3o, which allows us to obtain the angles for the different shapes of MoS_2 flakes in Figure 3i–n easily. The angles are listed in Table S4 (Supporting Information). In order to interpret the growth mechanism of MOCVD-grown MoS_2 through quantitative analysis, we project the six different sulfur flow rates with the fixed Mo concentration and the position of 0.7 cm (Figure 3i–n; position of 0 cm is at the edge of the furnace in the upstream location shown in Figure S2 (Supporting Information)) on an arctangent curve in Figure 3p. The *y*-axis is the arctangent for the angles with the range from $\pi/2$ to $\pi/2$; the *x*-axis indicates the logarithm of sulfur flow rate based on the experimental parameters. Among all the experimental data, five S-terminated points are used for analytical fitting and two Mo-terminated is used for validation. The reason for using arctangent function ($y = \arctan(x)$) is that it provides a domain of x for all real numbers and the range of principal value of $-\pi/2 < y < \pi/2$, which can connect all range of sulfur flow rate to the angles of MoS_2 shapes. Through the fitting data from Figure 3i–n, the best-fitted parameters for the arctangent curve are $[S_0] = 1.15$ and $\gamma = 0.2326$ as

$$\text{arct} = \frac{\log([S]/[S_0])}{\gamma} = \frac{\log([S]/1.15)}{0.2326} \tag{5}$$

Here, Equation (5) shows a similar expression of Cauchy distribution that the balanced sulfur concentration $[S_0]$ indicates the sulfur flow rate for regular hexagons of MoS_2. γ is equal to half the interquartile range, which is related to the sensitivity of sulfur concentration in the growth condition. A smaller γ indicates a narrower recipe window. The fitted results for S-terminated MoS_2 are shown in the upper half panel of Figure 3p. The model shows an excellent coefficient of determination ($R^2 = 0.9970$), which can well describe the growth behavior in a sulfur-rich synthesis environment. Moreover, we can predict the sulfur-deficit flowing rate of 1 sccm, 0.75 sccm, and 0.5 sccm for hexagon, equilateral triangle, and concave polygon Mo-terminated MoS_2, respectively. We used Figure 3n and Figure S7b (Supporting Information) as the validation data to confirm the prediction; the data points of 1 sccm and 0.75 sccm sulfur flowing rate in the lower half panel match well with the prediction. This analysis method provides us a better understanding of the growth system and the materials. For example, we can see that the region for S-terminated edges (the upper panel) contains more predicted points in Figure 3p, indicating a wider parameter window for growth. On the other hand, Mo-terminated MoS_2 (the lower panel) is relatively difficult to obtain based on our experiments and can be explained by this growth model. In order to confirm this analytic model in different Mo concentration, we also calculate the flakes geometry at the position of 1.3 cm and plot the results in Figure S14 (Supporting Information). Compared to Figure 3p at position of 0.7 cm, Figure S14 (Supporting Information) exhibits a higher temperature, indicating a higher Mo concentration. Therefore, the balanced sulfur concentration, $[S_0] = 1.28$ sccm, at position of 1.3 cm is slightly higher than at the position of 0.7 cm ($[S_0] = 1.15$ sccm). Furthermore, Figure S14 (Supporting Information) shows the smaller value γ of 0.0885, representing a narrower parameter window for the higher precursor condition with a faster chemical reaction. To confirm edge terminations, we identify the lattice orientation of MoS_2 flakes ($[S] = 1.25$ at 1.3 cm) by measuring the polarity of first-order conjugate peaks in the electron diffraction patterns[7,44] (Figure S8, Supporting Information). The result is consistent with our predictions in Figure S14 (Supporting Information). Our observation is consistent with previous experimental[8] and simulated[45] results that S-terminated MoS_2 shows a wider range of the precursor ratio (S/MoO_3) and dominates at lower temperatures due to the greater energy barrier of Mo sites with decreasing thermal energy (k_BT). Through this simple geometry calculation on different shapes of MoS_2 flakes, we can thus describe and predict the MoS_2 growth in the MOCVD process.

We characterize the crystal quality of our MOCVD MoS_2 grown at a low substrate temperature of 320 °C and compare the results with our oxide-based CVD-grown MoS_2 (>600 °C) in terms of strain, doping, and electronic performance. **Figure 4**a shows the deconvolution of strain and doping through the correlation analysis of A_{1g} and E_{2g} vibrational numbers. The as-grown CVD MoS_2 crystals typically show a higher biaxial tensile strain ($\varepsilon \approx 0.45\%$) due to the mismatch of the thermal expansion coefficient (TEC) between the MoS_2 film and the growth substrate during growth or cooling process from high temperature, as reported in the previous studies.[46,47] A high tensile strain in a MoS_2 crystal would reduce its bandgap with a rate of ≈100 meV per percent of biaxial strain or even lead to direct-to-indirect bandgap transition.[48,49] This strain issue could be mitigated using a low-temperature deposition process. As can be seen in Figure 4a, the built-in tensile strain is relaxed to ≈0.15% in the MOCVD monolayer MoS_2 crystals deposited with a low substrate temperature (blue dots). Furthermore, it is found that this low-temperature MOCVD-grown monolayer MoS_2 exhibits a lower electron doping compared to typical oxide-based CVD samples. Such unintentionally, highly n-type doping is common in oxide-based CVD-grown samples and could originate from structural defects, impurities, and substrate interaction at the interface,[46] which typically results in changes in photoluminescence (PL) characteristics due to the increased trion populations and nonradiative transitions.[50,51] Overall, both the built-in strain and the background electron doping are mitigated in the MOCVD MoS_2 crystals grown at a lower temperature. These influences together make our MOCVD-grown samples closer to the intrinsic point[46] characterized from the exfoliated counterpart in the previous study. Figure 4b shows the PL spectra of typical oxide-based CVD- and MOCVD-grown MoS_2, MOCVD-grown MoS_2 exhibits a narrower PL width with an energy close to the neutral A exciton due to the combined effects of the reduced strain and the lower portion of trion contribution (Figure S15, Supporting Information).[50,52] The characterization results suggest that high-quality monolayer MoS_2 can be obtained even with a low-substrate temperature of 320 °C through the proposed MOCVD growth mechanism.

The deposition temperature in our MOCVD is sufficiently low to enable a transfer-free process for the monolayer MoS_2 transistor fabrication (Figure 4c). This process allows

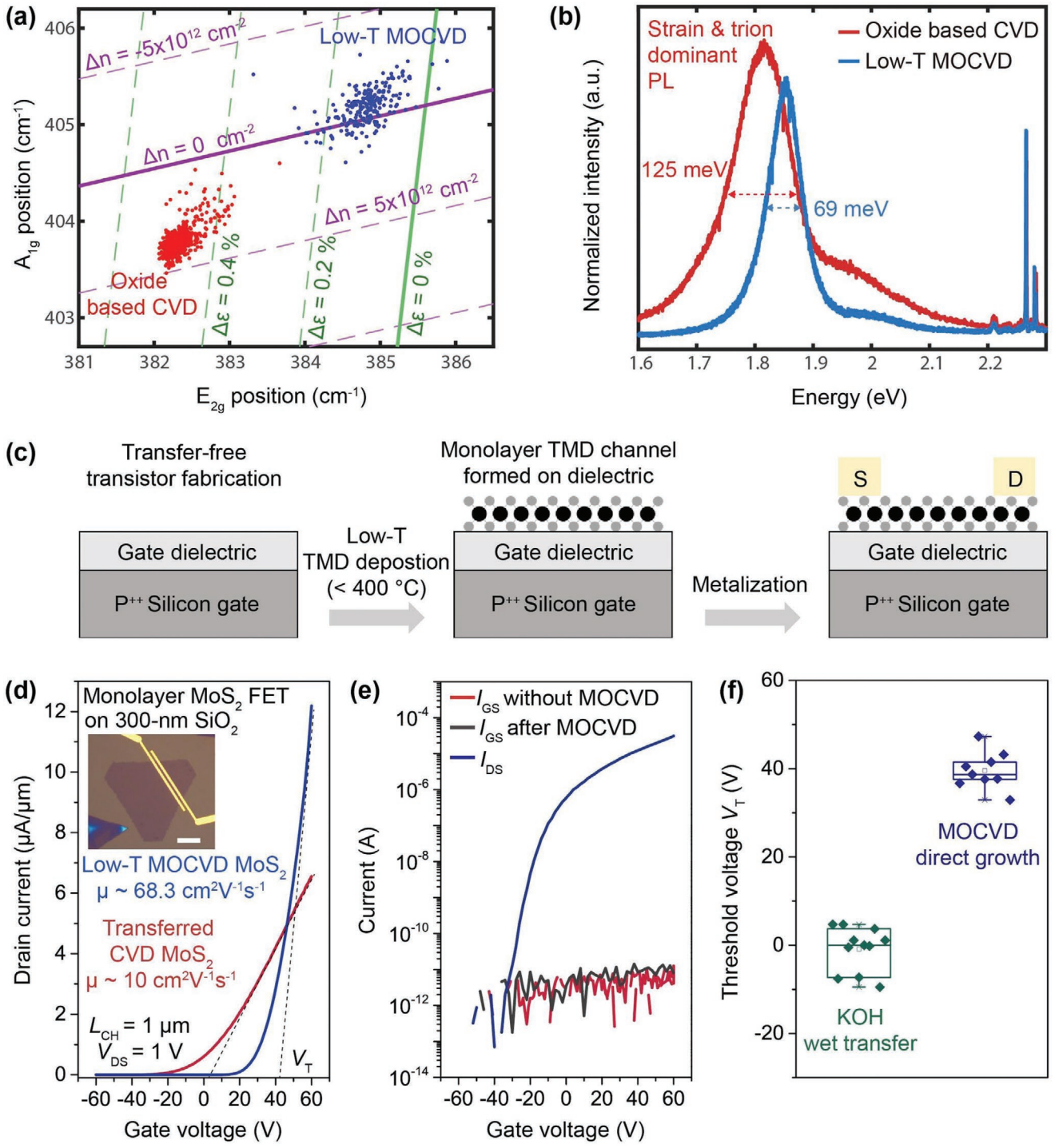

Figure 4. Optical and electrical characterizations of 320 °C low-substrate temperature-deposited MoS_2. a) The Raman-derived strain–charge doping (ε–n) maps and b) photoluminescence spectra of CVD monolayer MoS_2 grown at 625 °C (red) and low-temperature MOCVD monolayer MoS_2 grown at 320 °C (blue) on SiO_2/Si wafers. c) Schematic illustration of the fabrication process for transfer-free monolayer MoS_2 transistors. d) Transfer characteristics of monolayer MoS_2 FETs based on the CVD and MOCVD samples at $V_{DS} = 1$ V. Inset: Optical image of the MOCVD MoS_2 device (scale bar: 10 μm). e) Evaluation of back-gate-to-source leakage current (I_{GS}) flowing through the gate dielectric (300 nm thick SiO_2) used in the MOCVD MoS_2 FETs with and without the low-temperature MOCVD process. f) Comparison of the threshold voltages (V_T) of MOCVD MoS_2 FETs fabricated with and without the wet transfer process.

preserving the intrinsic properties of the as-grown MoS_2 such as carrier mobility. The low-strain characteristic in the low-temperature MOCVD-grown MoS_2 also suppresses the strain-induced electronic performance degradation.[53] As shown

in Figure 4d, the monolayer MoS_2 transistor exhibits a peak field-effect electron mobility as high as 68.3 $cm^2\ V^{-1}\ s^{-1}$ with an average of 20.4 $cm^2\ V^{-1}\ s^{-1}$ (Figure S16, Supporting Information) and an on/off ratio $>10^5$ at room temperature (Figure S17, Supporting Information), confirming a high quality of the deposited MoS_2 crystal. To the best of our knowledge, this electron mobility is the highest among the reported MOCVD-grown monolayer MoS_2 so far, and is noticeably higher than those in CVD-grown (≈10 $cm^2\ V^{-1}\ s^{-1}$) and other low-temperature ALD and sputtering (<1 $cm^2\ V^{-1}\ s^{-1}$) counterparts using the same gate dielectrics,[54–56] as summarized in Figure S20 (Supporting Information). We notice that the gate leakage current remains low (<10 pA) during the transistor operation, indicating no significant dielectric deteriorations caused by the low-temperature MOCVD process (Figure 4e). Note that high-temperature processes could produce leakage-current paths such as grain boundaries and oxygen vacancies in oxides materials.[10–12] In addition to the high-quality deposition discussed above, this high mobility in our monolayer MOCVD-grown MoS_2 could be attributed to the proposed transfer-free process. Since the monolayer MoS_2 channel is formed without involving transfer processes, scattering centers originating from either impurity residues (e.g., PMMA, KOH) or mechanical damages such as wrinkles, voids, and cracks can be significantly reduced. For instance, we note that there is a noticeable shift in the threshold voltage (V_T) between the MOCVD-grown MoS_2 transistors fabricated with and without the wet transfer process (Figure 4f; Figure S18, Supporting Information), which essentially suggests the variation in the electron doping level of the semiconductor channel before and after the transfer process and implies that the wet transfer process indeed affects the performance of the MoS_2 devices. Finally, the linear response of the output characteristics (I_{DS}-V_{DS}) indicates that a good electrical contact is formed on the low-temperature MOCVD-grown MoS_2 crystals (Figure S19, Supporting Information). Besides a clean contact interface,[57] theoretical studies have shown that a high density of structural defects such as sulfur vacancies in MoS_2 could degrade the contact performance (i.e., nonlinear output characteristics) and lead to an undesired high Schottky barrier at the metal-semiconductor interface as a result of metal-induced gap states.[58,59] Therefore, the observed linear, Ohmic-like output characteristics at room temperature in our monolayer MoS_2 FETs further confirm that high-quality 2D crystals with clean surfaces can be achieved through the demonstrated low-temperature, transfer-free process. Currently, the direct growth of MoS_2 on polymer substrates such as polyimide (PI) is still challenging for MOCVD due to the rough surface and the carbonization of the substrate (due to prolonged heating). Nevertheless, we consider this work has laid the foundation for the direct growth of MoS_2 on substrates that are sensitive to high temperatures and will spur future efforts to reduce the growth temperature even further.

3. Conclusion

In summary, we have demonstrated the preparation of high-quality MoS_2 with large domain size on various substrates by MOCVD method at low temperature, enabling nearly intrinsic MoS_2 with excellent electrical performances. Our approach not only paves the path toward fabrication of high-performance electronics and optoelectronics such as monolithic integrated circuits and photodetectors, but also opens up the possibility of direct synthesis of TMDs on low-thermal-budget substrates for emerging flexible/wearable devices. Moreover, we propose a model to quantitatively analyze the shape change of the MoS_2 flakes grown under different conditions, which provides an insight into the growth mechanism for optimizing growth conditions.

4. Experimental Section

Synthesis of Monolayer MoS_2: Monolayer MoS_2 was grown under low pressure by MOCVD. $Mo(CO)_6$ (98%, melting point T_m = 150 °C, boiling point T_b = 156 °C, Sigma Aldrich) and $(C_2H_5)_2S$ (98%, T_m = −103.8 °C, T_b = 92 °C, Sigma Aldrich) were selected as precursors of Mo and S, respectively. The precursors were supplied via a carrier gas (Argon) through a bubbler system into a one-inch quartz tube furnace. The optimized recipe for MoS_2 film is the flow rates of 100 sccm of Ar, 0.1 sccm of $Mo(CO)_6$, and 2.0 sccm of $(C_2H_5)_2S$ under the growth temperature of 320 °C (total pressure was 6.7 Torr).

Device Fabrication and Electrical Characterization: For those devices that involve a wet transfer process, monolayer MoS_2 was first transferred onto 300 nm SiO_2/p^{++}-Si substrates by standard PMMA/KOH wet transfer method. Standard electron-beam lithography and electron-beam evaporation followed by a liftoff process in hot acetone were used for source/drain patterning and metallization. All the electrical measurements were performed in a vacuum environment (10^{-5} to 10^{-6} torr) at room temperature in a Lakeshore probe station using an Agilent semiconductor parameter analyzer. The field-effect mobility of two-terminal MoS_2 devices studied in this work is calculated using $\mu = (dI_{DS}/dV_{BG}) \times [L_{CH}/(WC_{ox}V_{DS})]$, where I_{DS} is the drain current density, V_{BG} is the gate voltage, L_{CH} is the channel length, W is the channel width, and C_{ox} is the capacitance per unit area of the gate dielectric (1.15×10^{-8} F cm^{-2} for a 300 nm thick SiO_2).

Supporting Information

Supporting Information is available from the Wiley Online Library or from the author.

Acknowledgements

J.-H.P., A.-Y.L., and P.-C.S. contributed equally to this work. J.-H.P., A.-Y.L., P.-C.S., and J.K. acknowledge the U. S. Army Research Office through the Institute for Soldier Nanotechnologies at MIT under Cooperative Agreement No. W911NF-18-2-0048. J.-H.P., P.-C.S., and J.K. acknowledge the support from the U. S. Army Research Office (ARO) under Grant No. W911NF-18-1-0431. P.-C.S., H.W., and J.K. acknowledge the financial support from the Center for Energy Efficient Electronics Science (NSF Award No. 0939514). J.-H.P. was supported by the Postdoctoral Research Program of Sungkyunkwan University (2017). N.M. and J.K. acknowledge U.S. Department of Energy (DOE), Office of Science, Basic Energy Sciences (BES) under Award DE-SC0020042 and the support by the Air Force Office of Scientific Research under the MURI-FATE program, Grant No. FA9550-15-1-0514. R.X., D.H., and J.K. acknowledge the support by the National Science Foundation STC Center for Integrated Quantum Materials under Contract DMR-1231319. Y.H. acknowledges the use of the TEM facility at the Electron Microscopy Center (EMC) of Rice University.

Conflict of Interest

The authors declare no conflict of interest.

Keywords

2D materials, growth mechanisms, low-temperature deposition, MOCVD, MoS_2

Received: August 13, 2020
Revised: November 4, 2020
Published online:

[1] W. Wu, L. Wang, Y. Li, F. Zhang, L. Lin, S. Niu, D. Chenet, X. Zhang, Y. Hao, T. F. Heinz, J. Hone, Z. L. Wang, *Nature* **2014**, *514*, 470.
[2] E. Singh, P. Singh, K. S. Kim, G. Y. Yeom, H. S. Nalwa, *ACS Appl. Mater. Interfaces* **2019**, *11*, 11061.
[3] B. Radisavljevic, M. B. Whitwick, A. Kis, *ACS Nano* **2011**, *5*, 9934.
[4] Z. Yin, H. Li, H. Li, L. Jiang, Y. Shi, Y. Sun, G. Lu, Q. Zhang, X. Chen, H. Zhang, *ACS Nano* **2012**, *6*, 74.
[5] Q. Wan, M. T. Sharbati, J. R. Erickson, Y. Du, F. Xiong, *Adv. Mater. Technol.* **2019**, *4*, 1900037.
[6] S. Najmaei, Z. Liu, W. Zhou, X. Zou, G. Shi, S. Lei, B. I. Yakobson, J.-C. Idrobo, P. M. Ajayan, J. Lou, *Nat. Mater.* **2013**, *12*, 754.
[7] A. M. van der Zande, P. Y. Huang, D. A. Chenet, T. C. Berkelbach, Y. You, G.-H. Lee, T. F. Heinz, D. R. Reichman, D. A. Muller, J. C. Hone, *Nat. Mater.* **2013**, *12*, 554.
[8] S. Wang, Y. Rong, Y. Fan, M. Pacios, H. Bhaskaran, K. He, J. H. Warner, *Chem. Mater.* **2014**, *26*, 6371.
[9] J. Jiang, K. Parto, W. Cao, K. Banerjee, *IEEE J. Electron Devices Soc.* **2019**, *7*, 878.
[10] X. Zhu, F. Zhuge, M. Li, K. Yin, Y. Liu, Z. Zuo, B. Chen, R.-W. Li, *J. Phys. D: Appl. Phys.* **2011**, *44*, 415104.
[11] K. McKenna, A. Shluger, V. Iglesias, M. Porti, M. Nafría, M. Lanza, G. Bersuker, *Microelectron. Eng.* **2011**, *88*, 1272.
[12] H. Huff, D. Gilmer, *High Dielectric Constant Materials: VLSI MOSFET Applications*, Springer Science & Business Media, Berlin **2006**.
[13] C. Ahn, J. Lee, H.-U. Kim, H. Bark, M. Jeon, G. H. Ryu, Z. Lee, G. Y. Yeom, K. Kim, J. Jung, Y. Kim, C. Lee, T. Kim, *Adv. Mater.* **2015**, *27*, 5223.
[14] J. Mun, Y. Kim, I.-S. Kang, S. K. Lim, S. J. Lee, J. W. Kim, H. M. Park, T. Kim, S.-W. Kang, *Sci. Rep.* **2016**, *6*, 21854.
[15] Y. Zhao, J.-G. Song, G. H. Ryu, K. Y. Ko, W. J. Woo, Y. Kim, D. Kim, J. H. Lim, S. Lee, Z. Lee, J. Park, H. Kim, *Nanoscale* **2018**, *10*, 9338.
[16] H.-U. Kim, M. Kim, Y. Jin, Y. Hyeon, K. S. Kim, B.-S. An, C.-W. Yang, V. Kanade, J.-Y. Moon, G. Y. Yeom, D. Whang, J.-H. Lee, T. Kim, *Appl. Surf. Sci.* **2019**, *470*, 129.
[17] H.-Y. Cho, T. K. Nguyen, F. Ullah, J.-W. Yun, C. K. Nguyen, Y. S. Kim, *Phys. B* **2018**, *532*, 84.
[18] R. Frisenda, E. Navarro-Moratalla, P. Gant, D. P. De Lara, P. Jarillo-Herrero, R. V. Gorbachev, A. Castellanos-Gomez, *Chem. Soc. Rev.* **2018**, *47*, 53.
[19] K. Kang, K.-H. Lee, Y. Han, H. Gao, S. Xie, D. A. Muller, J. Park, *Nature* **2017**, *550*, 229.
[20] K. M. McCreary, A. T. Hanbicki, S. Singh, R. K. Kawakami, G. G. Jernigan, M. Ishigami, A. Ng, T. H. Brintlinger, R. M. Stroud, B. T. Jonker, *Sci. Rep.* **2016**, *6*, 35154.
[21] Z. Lin, Y. Zhao, C. Zhou, R. Zhong, X. Wang, Y. H. Tsang, Y. Chai, *Sci. Rep.* **2015**, *5*, 18596.
[22] K. Kang, S. Xie, L. Huang, Y. Han, P. Y. Huang, K. F. Mak, C.-J. Kim, D. Muller, J. Park, *Nature* **2015**, *520*, 656.
[23] H. Kim, D. Ovchinnikov, D. Deiana, D. Unuchek, A. Kis, *Nano Lett.* **2017**, *17*, 5056.
[24] S. H. Choi, B. Stephen, J.-H. Park, J. S. Lee, S. M. Kim, W. Yang, K. K. Kim, *Sci. Rep.* **2017**, *7*, 1983.
[25] K. Zhang, B. M. Bersch, F. Zhang, N. C. Briggs, S. Subramanian, K. Xu, M. Chubarov, K. Wang, J. O. Lerach, J. M. Redwing, S. K. Fullerton-Shirey, M. Terrones, J. A. Robinson, *ACS Appl. Mater. Interfaces* **2018**, *10*, 40831.
[26] C. C. Cho, S. L. Bernasek, *J. Appl. Phys.* **1989**, *65*, 3035.
[27] Z. Jin, S. Shin, D. H. Kwon, S.-J. Han, Y.-S. Min, *Nanoscale* **2014**, *6*, 14453.
[28] F. Maury, F.-D. Duminica, F. Senocq, *Chem. Vap. Deposition* **2007**, *13*, 638.
[29] I. Usoltsev, R. Eichler, Y. Wang, J. Even, A. Yakushev, H. Haba, M. Asai, H. Brand, A. Di Nitto, C. E. Düllmann, F. Fangli, W. Hartmann, M. Huang, E. Jäger, D. Kaji, J. Kanaya, Y. Kaneya, J. Khuyagbaatar, B. Kindler, J. V. Kratz, J. Krier, Y. Kudou, N. Kurz, B. Lommel, S. Miyashita, K. Morimoto, K. Morita, M. Murakami, Y. Nagame, H. Nitsche, K. Ooe, T. K. Sato, M. Schädel, J. Steiner, P. Steinegger, T. Sumita, M. Takeyama, K. Tanaka, A. Toyoshima, K. Tsukada, A. Türler, Y. Wakabayashi, N. Wiehl, S. Yamaki, Z. Qin, *Radiochim. Acta* **2016**, *104*, 141.
[30] J. Shi, D. Ma, G.-F. Han, Y. Zhang, Q. Ji, T. Gao, J. Sun, X. Song, C. Li, Y. Zhang, X.-Y. Lang, Y. Zhang, Z. Liu, *ACS Nano* **2014**, *8*, 10196.
[31] A. Q. Tool, J. B. Saunders, *J. Res. Natl. Bur. Stand.* **1949**, *42*, 171.
[32] Y.-H. Lee, L. Yu, H. Wang, W. Fang, X. Ling, Y. Shi, C.-T. Lin, J.-K. Huang, M.-T. Chang, C.-S. Chang, M. Dresselhaus, T. Palacios, L.-J. Li, J. Kong, *Nano Lett.* **2013**, *13*, 1852.
[33] X. Ling, Y.-H. Lee, Y. Lin, W. Fang, L. Yu, M. S. Dresselhaus, J. Kong, *Nano Lett.* **2014**, *14*, 464.
[34] K. Leng, Z. Chen, X. Zhao, W. Tang, B. Tian, C. T. Nai, W. Zhou, K. P. Loh, *ACS Nano* **2016**, *10*, 9208.
[35] H. Li, Q. Zhang, C. C. R. Yap, B. K. Tay, T. H. T. Edwin, A. Olivier, D. Baillargeat, *Adv. Funct. Mater.* **2012**, *22*, 1385.
[36] C. Lee, H. Yan, L. E. Brus, T. F. Heinz, J. Hone, S. Ryu, *ACS Nano* **2010**, *4*, 2695.
[37] B. G. Shin, G. H. Han, S. J. Yun, H. M. Oh, J. J. Bae, Y. J. Song, C.-Y. Park, Y. H. Lee, *Adv. Mater.* **2016**, *28*, 9378.
[38] S. Chen, J. Gao, B. M. Srinivasan, G. Zhang, V. Sorkin, R. Hariharaputran, Y.-W. Zhang, *npj Comput. Mater.* **2019**, *5*, 28.
[39] H. Kim, C. Mattevi, M. R. Calvo, J. C. Oberg, L. Artiglia, S. Agnoli, C. F. Hirjibehedin, M. Chhowalla, E. Saiz, *ACS Nano* **2012**, *6*, 3614.
[40] M. Ohring, *The Materials Science of Thin Films*, Academic Press, New York **1992**.
[41] A. Kobayashi, M. Steinberg, *The Thermal Decomposition of Methane in a Tubular Reactor*, Brookhaven National Laboratory (BNL), New York **1992**.
[42] S. Y. Yang, G. W. Shim, S.-B. Seo, S.-Y. Choi, *Nano Res.* **2017**, *10*, 255.
[43] J. Wang, X. Cai, R. Shi, Z. Wu, W. Wang, G. Long, Y. Tang, N. Cai, W. Ouyang, P. Geng, B. N. Chandrashekar, A. Amini, N. Wang, C. Cheng, *ACS Nano* **2018**, *12*, 635.
[44] P. Deb, M. C. Cao, Y. Han, M. E. Holtz, S. Xie, J. Park, R. Hovden, D. A. Muller, *Ultramicroscopy* **2020**, *215*, 113019.
[45] A. Govind Rajan, J. H. Warner, D. Blankschtein, M. S. Strano, *ACS Nano* **2016**, *10*, 4330.
[46] W. H. Chae, J. D. Cain, E. D. Hanson, A. A. Murthy, V. P. Dravid, *Appl. Phys. Lett.* **2017**, *111*, 143106.
[47] A. Michail, N. Delikoukos, J. Parthenios, C. Galiotis, K. Papagelis, *Appl. Phys. Lett.* **2016**, *108*, 173102.
[48] H. J. Conley, B. Wang, J. I. Ziegler, R. F. Haglund Jr., S. T. Pantelides, K. I. Bolotin, *Nano Lett.* **2013**, *13*, 3626.
[49] D. Lloyd, X. Liu, J. W. Christopher, L. Cantley, A. Wadehra, B. L. Kim, B. B. Goldberg, A. K. Swan, J. S. Bunch, *Nano Lett.* **2016**, *16*, 5836.

[50] D.-H. Lien, S. Z. Uddin, M. Yeh, M. Amani, H. Kim, J. W. Ager 3rd, E. Yablonovitch, A. Javey, *Science* **2019**, *364*, 468.
[51] S. Mouri, Y. Miyauchi, K. Matsuda, *Nano Lett.* **2013**, *13*, 5944.
[52] G. H. Ahn, M. Amani, H. Rasool, D.-H. Lien, J. P. Mastandrea, J. W. Ager Iii, M. Dubey, D. C. Chrzan, A. M. Minor, A. Javey, *Nat. Commun.* **2017**, *8*, 608.
[53] M. Amani, M. L. Chin, A. L. Mazzoni, R. A. Burke, S. Najmaei, P. M. Ajayan, J. Lou, M. Dubey, *Appl. Phys. Lett.* **2014**, *104*, 203506.
[54] J. Zhang, H. Yu, W. Chen, X. Tian, D. Liu, M. Cheng, G. Xie, W. Yang, R. Yang, X. Bai, D. Shi, G. Zhang, *ACS Nano* **2014**, *8*, 6024.
[55] R. Browning, P. Padigi, R. Solanki, D. J. Tweet, P. Schuele, D. Evans, *Mater. Res. Express* **2015**, *2*, 035006.
[56] J.-H. Huang, H.-H. Chen, P.-S. Liu, L.-S. Lu, C.-T. Wu, C.-T. Chou, Y.-J. Lee, L.-J. Li, W.-H. Chang, T.-H. Hou, *Mater. Res. Express* **2016**, *3*, 065007.
[57] C. D. English, G. Shine, V. E. Dorgan, K. C. Saraswat, E. Pop, *Nano Lett.* **2016**, *16*, 3824.
[58] D. Somvanshi, S. Kallatt, C. Venkatesh, S. Nair, G. Gupta, J. K. Anthony, D. Karmakar, K. Majumdar, *Phys. Rev. B* **2017**, *96*, 205423.
[59] J. Su, L. Feng, Y. Zhang, Z. Liu, *Appl. Phys. Lett.* **2017**, *110*, 161604.